A New Edge Element Analysis of Dispersive Waveguiding Structures

Jilin Tan and Guangwen Pan, *Senior Member, IEEE*

Abstract—**A new functional is rigorously selected for the edge element method to solve the $2-D\frac{1}{2}$ guided wave problems. The variational formulation is derived from the vector wave equation without any assumption or simplifications, and therefore the formulation is the full-wave analysis. Moderate to heavy ohmic loss and dielectric loss are taken into account in a natural and consistent manner. As a result, finite cross-section of arbitrary shape and finite conductivity can be handled without imposing the impedance boundary condition (IBC). The IBC may no longer be held for high-speed microelectronics applications, where the cross-section dimension may have been in the same order of the skin depths of some frequency components. The propagation modes are obtained by solving the large scale generalized eigenvalue and eigenvector equations employing the subspace iteration method. The spurious modes are totally suppressed in the whole frequency range of interest. Numerical examples of dielectric waveguide, microstrip transmission lines with finite conductivity are conducted and compared with previous publications with good agreement.**

I. Introduction

During the past decade the state-of-the-art integrated circuit technology has allowed the chip and the system clock rates to increase dramatically. In the case of CMOS, clock rates at the chip level have increased from 2–5 MHz in the early 1980's, to above 330 MHz in 1994. Silicon emitter coupled logic (ECL) clock rates have increased from 50 MHz in 1975 to the GHz range currently. Gallium Arsenide (GaAs) chips of 6–8 GHz clock rates have recently become feasible, with operating clock rates in excess of 10 GHz heterojunction bipolar transistor (HBT) cell and gate-array of over 500 usable gates promised for the mid-1990's. The advanced fabrication technology also allows the designer to form a much higher density system. The GaAs E/D MESFET processes can achieve 350–450 K gates per chip, the faster GaAs MESFET technologies achieve 10–50 K gates per chip, and the chip clock rates are as high as 2–2.5 GHz [1]. The cross section of the metal traces of the multichip modules (MCM's) is typically in the dimension of $5\mu \times 8\mu$, which is in the range of the skin depth of the metal for the low frequency components of the signal. The dc resistance of such structures of copper is typically 400 ohms per meter. The high speed (GHz), high density VLSI digital circuits and MMIC's inevitably cause signal distortion due to multiple reflection, uniplannar and multilayer crosstalk, skin effect, dispersion, and leaky phenomenon in the chip, packaged and unpackaged circuit board, and system levels. Therefore, the design of the packaging and interconnects is as important as the design of the integrated circuits themselves. Recently, extremely lossy dielectrics with loss tangent in the order of 10^5 have also found application in electronic systems. In CMOS circuits, the gate regions of the MOS transistors are usually doped heavily. In the bulk CMOS IC, the metal interconnects are deposited above these heavily doped substrates, which however results in a high line to substrate capacitance. The nonwork power has then to be increased to charging these capacitance proportionally. The fore-knowledge of these effects are therefore needed for successful system design and to optimize performance.

High speed interconnect effects are usually simulated by lumped and distributed circuits models of multiconductors with electrical equivalent parameters of the network. The parameters, including capacitance, inductance, resistance, conductance matrices are usually obtained by the quasi-static analysis in conjunction with the small perturbation method [2]–[5]. With $\leq$100 picosecond rising time and GHz bandwidth, the quasi-static assumption is not generally held. This is because the electrical characteristics, represented by the dispersion, line losses, which are all frequency dependent, have to be modeled accurately. The small perturbation method may no longer be applicable because none of the losses, neither ohmic nor dielectric, are small. Besides the difficulty in modeling the lossy dielectric accurately and dynamically, describing the behavior of the conductors with finite thickness and finite conductivity is another obstacle in extracting these parameters. The hybrid mode analysis has been used to extract circuit parameters, including characteristic impedance, propagation constant, and attenuation factor by taking into account the dispersion effects for high speed circuits [6], [7]. In their approaches, the lossy conductors are treated with complex surface impedances. This approximation is able to yield quite satisfactory results for narrow banded MMIC's at higher frequencies with thicker conductors, where the skin depth is much smaller than the conductor thickness. Nonetheless, for the thin conductor problems encountered in MCM's, this method is not valid for the whole frequency spectrum of interest. In fact, the skin depths of the metal for the lower spectrum portion may be greater than the metal thickness. Kiang *et al.* proposed the volume integral equation method (VIE) to solve the dispersive transmission line problems [8]. In theory, the VIE is rigorous. However, due to mathematical instability in searching the roots, which correspond to the

Manuscript received January 16, 1995; revised August 1, 1995. This work was supported in part by DARPA/ESTO Grant N00014-91-J-4030 from the Office of Naval Research and Boeing Aerospace Co. Contract 133-P771.

The authors are with the Department of Electrical Engineering, Arizona State University, Tempe, AZ 85287-7206 USA.

IEEE Log Number 9414845.

complex propagation constants of the fundamental and higher modes, the results of this method is good only within a few GHz for typical MCM geometries. The surface integral equation method (SIE) has been successfully applied to the problems of this category as well [9]. But the limitation is that the dielectric structure must be layered because the Green's functions in the SIE are derived for layered media. On many occasions, the substrate interface may have grooves or notches of irregular shapes, which prevent the SIE from direct applications.

The finite element method (FEM) is attractive because of its systematic procedure and its flexibility to any complicated geometries and boundary conditions [10], [11]. As far as the $2-D\frac{1}{2}$ dielectric loaded waveguide structure is concerned, node based FEM has successfully been used [12], [13]. These approaches, however, can not be directly applied to transmission lines with finite thickness and finite conductivity because of the appearance of "spurious modes." In fact, the conventional node based FEM can not be employed in the field domain in which material property changes abruptly [14]. As a result, the "vector element" or edge FEM has emerged aiming to solve the dielectric and conductor interface problems [10], [15], [16]. With degrees of freedom associated with edges of the mesh, the edge FEM guarantees the continuity of the tangential field components across interfaces without imposing any of the normal field quantities. In [15] the vector element has been applied to the lossless waveguide structures with great success. However, the functional employed in the paper does not take any losses, dielectric, ohmic or radiative, into account. Based on [15], a new approach has been proposed, which handles dielectric loss in waveguide structures [17]. In the approach, the vector Helmholtz equation is decomposed into two coupled partial differential equations. Taking the inner product of the corresponding vector components, the functional was then constructed by subtracting the second equation from the first ((5) in [17]). The trial function and test function were chosen to be the same, namely, the electric field. The functional in that paper is correct, and effective. But the derivation of the functional seems not to be systematic, because one can ask why subtracting the second equation from first, instead of adding them together.

In the current paper we provide a rigorous and systematic construction of the functional for the general $2-D\frac{1}{2}$ structures by using the 3-D vector form. The boundary conditions of the first, second, and third kind are all taken into account. Thus, the functional characterizes a wide range of the $2-D\frac{1}{2}$ waveguiding structures. The functional takes the previous two functionals of the previous two papers as its special cases. Employing the edge element method and utilizing the new functional, we have solved the general waveguiding problem of conductors with finite conductivity and cross section in a lossy dielectric media. For thin conductor cases where the impedance condition does not apply, one can mesh the grids into the interior of the conductors. Several transmission line structures have been attacked and the numerical results are presented.

The remainder of the paper is organized as follows: Section II, III, IV present the basic theory, followed by the edge element procedure of Section V. Numerical examples are provided in Section VI.

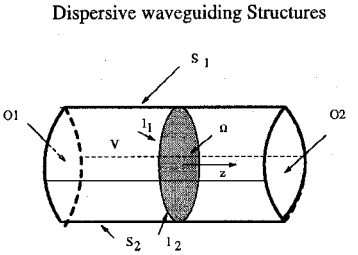

Fig. 1. Waveguiding structure.

II. New Functional Formulation

In this section, we present a rigorous derivation of the required functional for waveguiding structures in an isotropic and piecewise homogeneous environment. This derivation can easily be generalized to anisotropic and inhomogeneous cases.

We begin with the vector wave equation

$$\nabla \times \frac{1}{\mu_r} \nabla \times \vec{E} - \epsilon_r k_0^2 \vec{E} = 0 \quad \text{on } V \tag{1}$$

where the wavenumber $k_0 = \omega\sqrt{\mu_0 \epsilon_0}$, μ_0 and ϵ_0 are the free space permeability and permittivity of the material, respectively, and V denotes the solution domain, as depicted in Fig. 1. Note that in (1), the solution domain of the 3-D vector wave equation is defined in a volume region as shown in Fig. 1, instead of just the cross section Ω of the waveguide structure as specified in [15].

The homogeneous boundary conditions are given in [11] as

$$\begin{cases} \hat{n} \times \vec{E} = 0 & \text{on } S_1 \quad \text{(2a)} \\ \frac{1}{\mu_r} \hat{n} \times \nabla \times \vec{E} + \gamma_e \hat{n} \times \hat{n} \times \vec{E} = 0 & \text{on } S_2 \quad \text{(2b)} \end{cases}$$

where $S = S_1 \cup S_2$, and γ_e is a frequency dependent parameter as will be given in (15).

Judiciously selecting the adjoint field $\vec{E}^\dagger$ and taking the inner product with the left hand side of (1), we have

$$F(\vec{E}) = \int_V \left[(\nabla \times \vec{E}^\dagger) \frac{1}{\mu_r} \cdot (\nabla \times \vec{E}) - \epsilon_r k_0^2 (\vec{E}^\dagger \cdot \vec{E}) \right] dv - \oint_{S+O1+O2} \left[\vec{E}^\dagger \times \frac{1}{\mu_r} \nabla \times \vec{E} \right] \cdot d\vec{s}. \tag{2}$$

Upon applying the boundary condition (2a), (2b), (2) can be deduced as

$$F(\vec{E}) = \int_V \left[(\nabla \times \vec{E}^\dagger) \frac{1}{\mu_r} \cdot (\nabla \times \vec{E}) - \epsilon_r k_0^2 (\vec{E}^\dagger \cdot \vec{E}) \right] dv + \gamma_e \int_{S2} [\hat{n} \times \vec{E}^\dagger] \cdot [\hat{n} \times \vec{E}] ds - \int_{O1+O2} \left[\vec{E}^\dagger \times \frac{1}{\mu_r} \nabla \times \vec{E} \right] \cdot d\vec{s}. \tag{3}$$

For the exact solution of the electrical field, the functional $F(\vec{E}) = 0$.

Since the solution domain can be arbitrarily chosen along the wave propagation direction $\vec{z}$, in which the structure is uniform and is extended to $\pm\infty$, the functional per unit length

must be independent of the portion along the $\vec{z}$ axis. Therefore, the integrations over $O1$ and $O2$ ought to cancel each other. As a result, the sufficient and necessary condition to achieve the cancellation is to specify the adjoint field $\vec{E}^{\dagger}$. The physical meaning of such a choice is to employ the adjoint field which propagates in the opposite direction of the original field $\vec{E}$. According to [18] or [19], the relation between the two fields can be expressed as

$$\begin{aligned}\vec{E} &= (\vec{E}_t + \hat{z}E_z)e^{-\gamma z}\\ \vec{E}^{\dagger} &= (\vec{E}_t - \hat{z}E_z)e^{\gamma z}.\end{aligned} \tag{4}$$

Hence, we arrive at

$$\begin{aligned}F_p(\vec{E}) = &\int (\nabla \times \vec{E}^{\dagger})\frac{1}{\mu_r}\cdot(\nabla\times\vec{E})\,d\Omega - k_0^2\int \epsilon_r\vec{E}^{\dagger}\cdot\vec{E}\,d\Omega\\ &+\gamma_e\int_{l_2}(\hat{n}\times\vec{E}^{\dagger})\cdot(\hat{n}\times\vec{E})\,dl\end{aligned} \tag{5}$$

where the F_p is the functional per unit length and $l = l_1 \cup l_2$, is the contour of the cross section Ω as shown in Fig. 1. Noticing

$$\begin{aligned}\nabla\times\vec{E}^{\dagger}\cdot\nabla\times\vec{E} &= \nabla_t\times\vec{E}_t\cdot\nabla_t\times\vec{E}_t\\ &\quad -(\gamma\vec{E}_t+\nabla_t E_z)\cdot(\gamma\vec{E}_t+\nabla_t E_z)\\ \vec{E}^{\dagger}\cdot\vec{E} &= \vec{E}_t\cdot\vec{E}_t - E_z\cdot E_z\end{aligned} \tag{6}$$

where $\nabla_t = \hat{x}\frac{\partial}{\partial x} + \hat{y}\frac{\partial}{\partial y}$. Introducing new variables

$$\begin{aligned}E_z &= \gamma e_z\\ \vec{E}_t &= \vec{e}_t\end{aligned}$$

we end with

$$\begin{aligned}F(\vec{e}) = &\int\left[\frac{1}{\mu_r}(\nabla_t\times\vec{e}_t)^2 - \epsilon_r k_0^2\vec{e}_t^2\right]d\Omega\\ &-\gamma^2\int\left[(\vec{e}_t+\nabla_t e_z)^2 - \epsilon_r k_0^2 e_z^2\right]d\Omega\\ &+\gamma_e\int_{s2}\left[(\hat{n}\times\vec{e}_t)^2 - \gamma^2 e_z^2\right]dS.\end{aligned} \tag{7}$$

Equation (7) is the desired form in obtaining the eigenvalues and eigenvectors of the general $2-D\frac{1}{2}$ dispersive waveguiding problems consisting of conductors of finite conductivity and finite cross sections in a lossy environment under the homogeneous boundary conditions. The nice property of this functional is its physical symmetry, which is a consequence of the fact that in a two dimensional structure the vector fields propagate in both directions without any preference.

It is worth mentioning that if the required adjoint field is applied to the solution domain of a cross section Ω as in [15], [17], [20], the adjoint field can only be chosen according to (1). In other words, the selections of $\vec{E}$, $\vec{E}^*$, $\vec{H}$ for adjoint are improper. To verify this statement, let us start from the vector wave (1). Following the previous procedures, except the domain now is on Ω instead of in V, we arrive at

$$\begin{aligned}F(\vec{E}) = &\int_{\Omega}\left[(\nabla_t\times\vec{E}_t^{\dagger})\frac{1}{\mu_r}\cdot(\nabla_t\times\vec{E}_t) - \epsilon_r k_0^2\vec{E}_t^{\dagger}\cdot\vec{E}_t\right]d\Omega\\ &+\int_{\Omega}\left[(\gamma^{\dagger}\vec{E}_t^{\dagger}+\nabla_t E_z^{\dagger})\frac{1}{\mu_r}\cdot(\gamma\vec{E}_t+\nabla_t E_z)\right.\\ &\left.-\epsilon_r k_0^2 E_z E_z^{\dagger}\right]d\Omega\end{aligned} \tag{8}$$

where $\gamma_e = 0$ is assumed for simplicity. In (8), the $\gamma^{\dagger}$ is the propagation constant of the adjoint field $\vec{E}^{\dagger}$. The Euler equations satisfying (8) are

$$\begin{aligned}\nabla_t\times\frac{1}{\mu_r}\nabla_t\times\vec{E}_t + \frac{\gamma^{\dagger}}{\mu_r}(\nabla_t E_z+\gamma\vec{E}_t) - \epsilon_r k_0^2\vec{E}_t = 0\\ \nabla_t\times\frac{1}{\mu_r}[(\nabla_t E_z+\gamma\vec{E}_t)\times\hat{z}] - \epsilon_r k_0^2 E_z\hat{z} = 0.\end{aligned} \tag{9}$$

On the other hand, the vector wave (1) can be directly decomposed into

$$\begin{aligned}\nabla_t\times\frac{1}{\mu_r}\nabla_t\times\vec{E}_t - \frac{\gamma}{\mu_r}(\nabla_t E_z+\gamma\vec{E}_t) - \epsilon_r k_0^2\vec{E}_t = 0\\ \nabla_t\times\frac{1}{\mu_r}[(\nabla_t E_z+\gamma\vec{E}_t)\times\hat{z}] - \epsilon_r k_0^2 E_z\hat{z} = 0.\end{aligned} \tag{10}$$

Comparing (10) with (9), we have

$$\gamma^{\dagger} = -\gamma. \tag{11}$$

For lossless cases, this condition degenerates back to

$$\gamma^{\dagger} = -j\beta \tag{12}$$

if γ is $j\beta$. The previous discussions can be extended to the inhomogeneous boundary conditions

$$\begin{cases}\hat{n}\times\vec{E} = \vec{P} & \text{on } S_1\\ \frac{1}{\mu_r}\hat{n}\times\nabla\times\vec{E} + \gamma_e\hat{n}\times\hat{n}\times\vec{E} = \vec{U} & \text{on } S_2\end{cases}. \tag{13}$$

The functional can be shown to be

$$\begin{aligned}I(\vec{E}) = &\int_{\Omega}\left[(\nabla\times\vec{E}^{\dagger})\frac{1}{\mu_r}\cdot(\nabla\times\vec{E}) - \epsilon_r k_0^2\vec{E}^{\dagger}\cdot\vec{E}\right]d\Omega\\ &+\gamma_e\int_{l_2}[\hat{n}\times\vec{E}^{\dagger}]\cdot[\hat{n}\times\vec{E}]dl\\ &+\int_{l_2}\left[\vec{U}^{\dagger}\cdot\vec{E}+\vec{U}\cdot\vec{E}^{\dagger}\right]dl.\end{aligned} \tag{14}$$

In (14), the integral of $\hat{n}\times\vec{E} = \vec{P}$ over l_1 as an invariant has been removed from the functional. However, it needs to be included in the implementation of fields computation procedures. To emphasize, we require $\gamma^{\dagger} = -\gamma$.

III. The Extended Third Boundary Condition

The third boundary condition (2b), can be used on many occasions. When the ground plane consists of imperfect conductors, the impedance boundary condition (2b) is applicable. In this case, the parameter

$$\gamma_e = jk_0\sqrt{\frac{\epsilon_{rc} - j\frac{\sigma}{\omega\epsilon_0}}{\mu_{rc}}} \tag{15}$$

where ϵ_{rc} is the relative permittivity and σ is the conductivity of the thick imperfect conductor. The use of this formula, however, is by no means of imperfect impedance condition only. In fact, (15) and (2b) in conjunction with the new functional (7) can be applied to:

1) The magnetic wall, by setting $\gamma_e = 0$.
2) The electrical wall, by setting $\gamma_e = \infty$.

In addition, the boundary condition of the third kind can be extended to an artificial boundary in the form of

$$\frac{1}{\mu_r}\hat{n}\times\nabla\times\vec{E}+\gamma_e\hat{n}\times\hat{n}\times\vec{E}+\hat{n}\times\tilde{\varphi}(\vec{E_n})=0 \tag{16}$$

where $\tilde{\varphi}$ is a linear operator. To be more specific, let us take a stripline case, where the structures are bounded between the upper and lower ground planes, separated by h. In the region far away from the strips, the fields behave mainly as TEM waves of

$$\begin{Bmatrix}\sin(\frac{\pi y}{h})e^{-(\frac{\pi}{h}x)}e^{-\gamma z}\\ \cos(\frac{\pi y}{h})e^{-(\frac{\pi}{h}x)}e^{-\gamma z}\end{Bmatrix} \tag{17}$$

where the higher order perturbation terms due to the conductor imperfectness have been neglected.

As the first order approximation, (17) is a good enough to derive the extended third kind boundary condition. For the electric fields of expression (17), it can be shown that

$$\frac{1}{\mu_r}\hat{n}\times\nabla\times\vec{E}=-\left(\frac{\pi}{\mu_r h}\right)\hat{n}\times\hat{n}\times\vec{E}+\frac{\gamma}{\mu_r}\hat{n}\times\hat{z}\times\vec{E}_n-\frac{1}{\mu_r}\hat{n}\times\hat{y}\times\frac{\partial\vec{E}_n}{\partial y}. \tag{18}$$

Comparing with (16), we have $\gamma_e=\frac{\pi}{\mu_r h}$, and

$$\tilde{\varphi}=\frac{\gamma}{\mu_r}\hat{z}\times-\frac{1}{\mu_r}\hat{y}\times\frac{\partial}{\partial y}. \tag{19}$$

Although (18) looks not exactly the same form as (2b), the additional terms have no contribution to the functional as far as the linear edge element implementation is concerned. In fact, only the tangential components, say $\vec{E}_t$, are needed for the boundary edges, while the normal components of the fields have no roles there. Therefore, the extended boundary condition (16) can be directly implemented under the new functional formulation. By applying (16) to the artificial boundaries, the mesh region will be reduced significantly. The effectiveness and correctness of this technique has been tested with great success as will be seen in Section VI of numerical examples.

IV. Characteristic Impedances

Besides the complex propagation constant, which can be evaluated using (7), the complex impedance is another useful parameter. For a $N+1$ transmission line system, there exist N propagation eigen modes, and the element of the power matrix is

$$P^{k,l}=\frac{j\gamma_l^*}{\omega\mu_r^*}\int\left[\vec{e}_t^{\,k}\cdot(\vec{e}_t^{\,l})^*+\vec{e}_t^{\,k}\cdot\nabla_t(e_z^l)^*\right]d\Omega \tag{20}$$

where $*$ denotes complex conjugate, k,l indicates mode k and mode l respectively. The current flowing on line i, corresponding to the kth mode, can be obtained from the Ohm's law in conjunction with the kth eigenvector, namely

$$I_i^k=\int_{\text{line }i}\vec{j}^{\,k}\cdot d\vec{\Omega}=\gamma^k\sigma\int_{\text{line }i}e_z^k d\Omega \tag{21}$$

where $\vec{j}^{\,k}$ is the current density vector on line i of mode k, $\vec{\Omega}$ is the area of the cross section of line i. The characteristic impedance matrix then is found to be [21]

$$Z_c=[I^{-1}]^{*T}P^TI^{-1} \tag{22}$$

where T is the transpose of a matrix, P is the power matrix and I is the current matrix.

V. Edge Element Procedure

The $\nabla\cdot\vec{D}=0$ condition is automatically satisfied by the vector wave (1). To apply the functional (7), we need to impose the condition $\nabla_t\cdot\vec{W}_t=0$ in the element construction, where $\vec{W}_t$ is the shape function such that

$$\vec{E}_t=\sum_{i=1}^{M}E_{ti}\vec{W}_{ti}. \tag{23}$$

For the 2-D dimensional structures, only two components of the vector fields are independent. Since E_z has been chosen as one independent variable, only one more independent variable has left to select out of the two tangential components in the domain Ω.

The most useful edge elements, which have been constructed thus far for the 2-D structures, are the rectangular vector element and the triangular vector element. Both algorithms satisfy the divergence free condition for the transverse field components. The shape functions for the rectangular vector element are [11]

$$\begin{aligned}\vec{W}_{t1}^e&=\frac{1}{l_y^e}\left(y_c^e+\frac{l_y^e}{2}-y\right)\vec{x}\\ \vec{W}_{t2}^e&=\frac{1}{l_y^e}\left(-y_c^e+\frac{l_y^e}{2}+y\right)\vec{x}\\ \vec{W}_{t3}^e&=\frac{1}{l_x^e}\left(x_c^e+\frac{l_x^e}{2}-x\right)\vec{y}\\ \vec{W}_{t4}^e&=\frac{1}{l_x^e}\left(-x_c^e+\frac{l_x^e}{2}+x\right)\vec{y}.\end{aligned} \tag{24}$$

The shape functions for the vector triangle element are

$$\begin{aligned}\hat{n}_1^e&=(L_1^e\nabla L_2^e-L_2^e\nabla L_1^e)l_1^e\\ \hat{n}_2^e&=(L_2^e\nabla L_3^e-L_3^e\nabla L_2^e)l_2^e\\ \hat{n}_3^e&=(L_3^e\nabla L_1^e-L_1^e\nabla L_3^e)l_3^e\end{aligned} \tag{25}$$

where l_i^e is used to normalize $\hat{n}_i^e$, and L_i^e are the area coordinates, which are defined as

$$\begin{bmatrix}L_i^e\\ L_j^e\\ L_k^e\end{bmatrix}=\frac{1}{2\Delta}\begin{pmatrix}a_i & b_i & c_i\\ a_j & b_j & c_j\\ a_k & b_k & c_k\end{pmatrix}\begin{bmatrix}1\\ x\\ y\end{bmatrix} \tag{26}$$

with $a_i=x_jy_k-x_ky_j$, $b_i=y_j-y_k$, $c_i=-(x_j-x_k)$. Similar relations hold for other coefficients. It has been shown that

$$L_i^e+L_j^e+L_k^e=1. \tag{27}$$

Letting $\xi_i = L_i$, then it can easily be verified that

$$I^e(\alpha,\beta,\gamma) = \int_\Delta \xi_i^\alpha \xi_j^\beta \xi_k^\gamma dxdy = 2\Delta \int_0^1 \xi_i^\alpha d\xi_i \int_0^{1-\xi_i} \xi_j^\beta (1-\xi_i-\xi_j)^\gamma d\xi_j = \frac{\alpha!\beta!\gamma!}{(\alpha+\beta+\gamma+2)!} 2\Delta. \tag{28}$$

The quadrilateral type of the vector elements is not recommended since it does not satisfy the divergence free condition.

Based on the analysis above, the fields can be written in the form of

$$\vec{e}_t^e = \sum_{i=1}^n \vec{W}_i^e e_{ti}^e$$
$$e_z^e = \sum_{i=1}^n B_i^e e_{zi}^e \tag{29}$$

where B_i^e are the conventional finite element shape functions. Finally, the functional in each element can be written as

$$F^e = \{e_t^e\}^T [A_{tt}^e]\{e_t^e\} - \gamma^2 \begin{Bmatrix} e_t^e \\ e_z^e \end{Bmatrix}^T \begin{bmatrix} B_{tt}^e & B_{tz}^e \\ B_{zt}^e & B_{zz}^e \end{bmatrix} \begin{Bmatrix} e_t^e \\ e_z^e \end{Bmatrix}. \tag{30}$$

The global functional can then be formed as

$$F = \sum_{e=1}^{Ne} F^e \tag{31}$$

$$= \begin{bmatrix} e_t \\ e_z \end{bmatrix}^T \begin{bmatrix} A_{tt} & 0 \\ 0 & 0 \end{bmatrix} \begin{bmatrix} e_t \\ e_z \end{bmatrix} - \gamma^2 \begin{bmatrix} e_t \\ e_z \end{bmatrix}^T \begin{bmatrix} B_{tt} & B_{tz} \\ B_{zt} & B_{zz} \end{bmatrix} \begin{bmatrix} e_t \\ e_z \end{bmatrix}. \tag{32}$$

At the stationary point, the first variation of (32) is zero, yielding

$$\begin{bmatrix} A_{tt} & 0 \\ 0 & 0 \end{bmatrix} \begin{bmatrix} e_t \\ e_z \end{bmatrix} - \gamma^2 \begin{bmatrix} B_{tt} & B_{tz} \\ B_{zt} & B_{zz} \end{bmatrix} \begin{bmatrix} e_t \\ e_z \end{bmatrix} = 0. \tag{33}$$

It is not an easy task to solve the eigen (33). There is no commercial solver available for the large scale, complex, generalized eigenvalue and eigenvector problems. The matrix size involved in (33) can easily reach a few thousand squared. and the number of the eigenvectors is also very huge. For the transmission line type structures, however, only a few eigenvalues, corresponding to the fundamental propagation modes, are essential to us. As a result, the subspace iteration method is extremely suitable for our applications.

The subspace iteration method is first proposed by K. Bathie, and the detail can be found in [22]. Recently, F. Fernandez solved a dielectric waveguide problem by using a modified subspace iteration method [23]. The basic procedures in solving the generalized eigenvalue problem

$$Ax = \lambda Bx \tag{34}$$

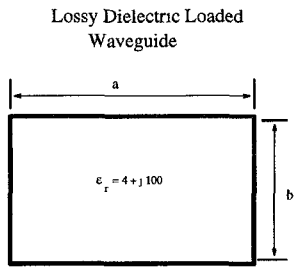

Fig. 2. Lossy dielectric loaded waveguide.

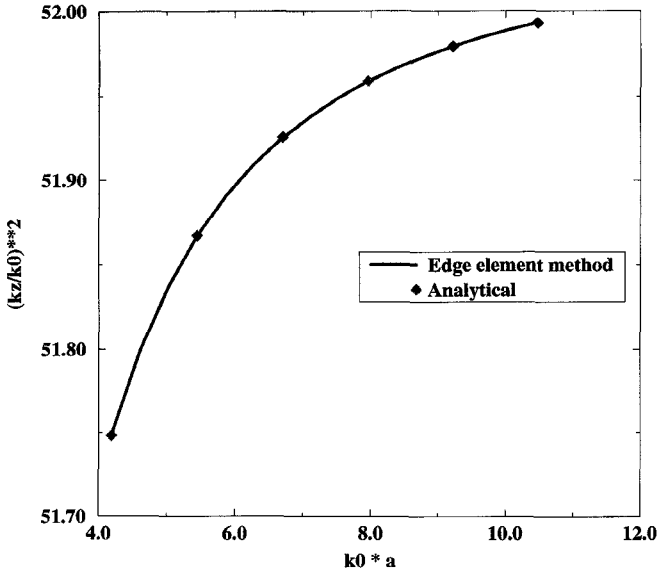

Fig. 3. Dispersion curve of the lossy dielectric loaded waveguide.

are briefly summarized as the follows. Let the dimension of A and B be $N \times N$, and the number of eigenvalues of interest be $p \ll N$. Thus, the iterative steps are

$$\begin{aligned} (A-\mu B)X^{s+1} &= BX^s \\ A^{s+1} &= [X^{s+1}]^t (A-\mu B) X^{s+1} \\ B^{s+1} &= [X^{s+1}]^t B X^{s+1} \\ A^{s+1}\Phi^{s+1} &= B^{s+1}\Phi^{s+1}\Gamma^{s+1}. \end{aligned} \tag{35}$$

The required eigenvectors and eigenvalues are, respectively

$$X = X^{s+1}\Phi^{s+1} \tag{36}$$

and

$$\lambda^{s+1}(i) = \gamma^{s+1}(i) + \mu \tag{37}$$

where $\gamma^{s+1}(i)$ is the ith element of the diagonal matrix Γ^{s+1}. By adjusting the shift factor μ, the subspace iteration method convergence quickly to the lowest eigenvalues.

Taking advantage of the sparsity of the matrix in finite element method, we have implemented the subspace iteration method in the edge element algorithm and successfully solved the eigenvalue and eigenvector problems for matrices of dimension in several thousands.

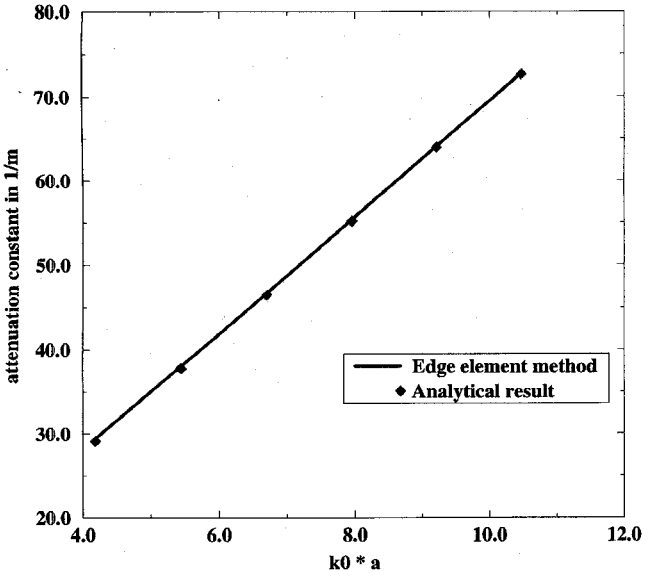

Fig. 4. Attenuation curve of the lossy dielectric loaded waveguide.

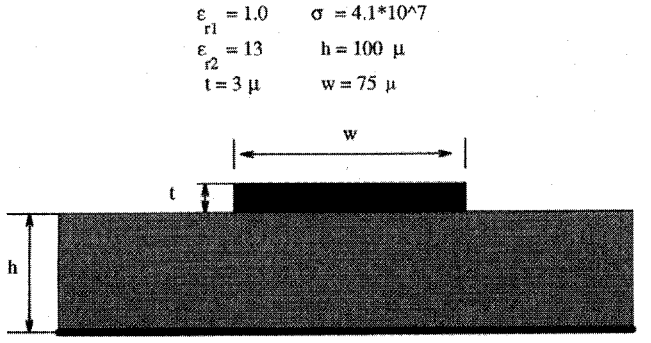

Fig. 5. Microstrip line with finite thickness and finite conductivity.

VI. Numerical Results

Numerical examples are provided to demonstrate the correctness and effectiveness of the new formulas, and to verify that the spurious modes have been totally suppressed.

Example 1—Lossy Dielectric Loaded Waveguide: A lossy dielectric loaded rectangular waveguide, as shown in Fig. 2, is presented here to verify our formulation and the numerical codes, since the analytical solution exists for this structure. The normalized complex propagation constant is well known to be

$$\sqrt{\epsilon_r - \left(\frac{m\pi}{k0 * a}\right)^2 - \left(\frac{n\pi}{k0 * b}\right)^2}.$$

Assuming $a = 2b = 1$ and $\epsilon_r = 4 + j100$, this means that the loss tangent equals 87°. The numerical values of the propagation constant and attenuation factor for the first mode are shown in Figs. 3 and 4.

Example 2—Microstrip Line with Finite Conductivity: Fig. 5 illustrates the configuration of a lossy microstrip line of 3 μm thick. Both the microstrip and the ground plane are lossy with $\sigma = 4.1 * 10^7$ for the signal line and $\sigma = 5.8 * 10^7$ s/m for the ground. The substrate can be lossy, however, here we assume it to be lossless with dielectric permittivity of $\epsilon_r = 13$.

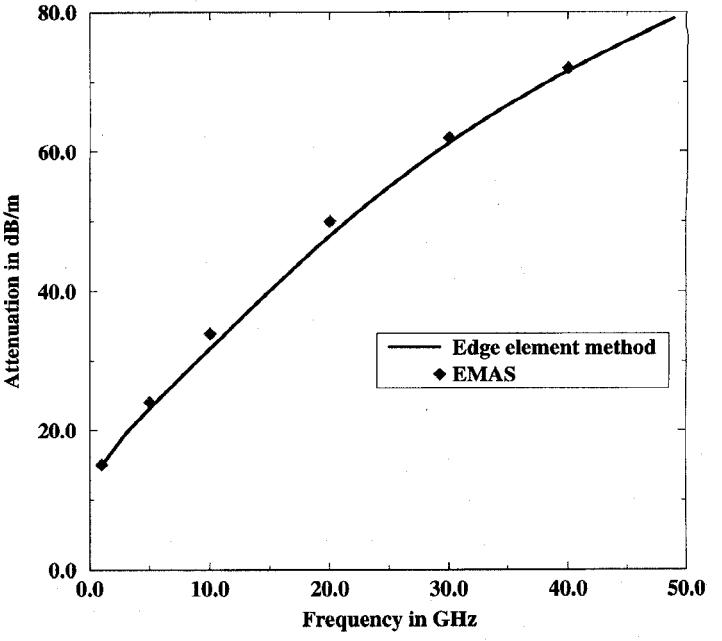

Fig. 6. Attenuation constant of the lossy microstrip line.

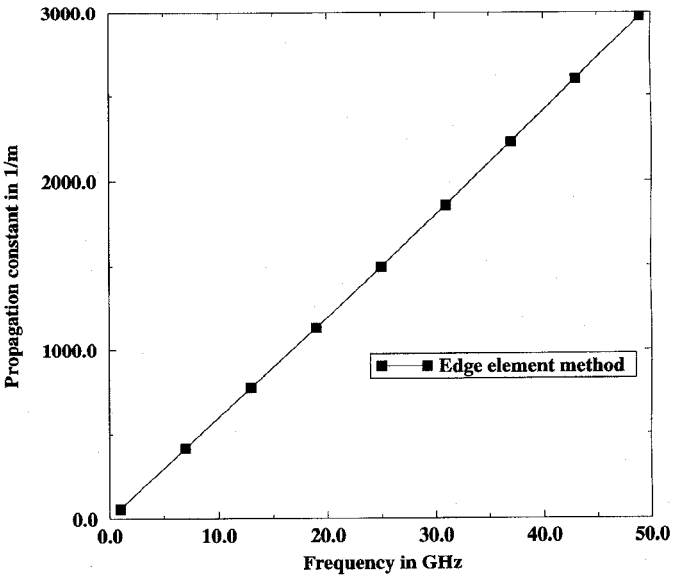

Fig. 7. Propagation constant of the lossy microstrip line.

In Fig. 6, we compare our results against a commercial software, EMAS [24] for the attenuation curve from 1 GHz to 40 GHz. Again agreement is reasonably good. Figs. 7, 8, and 9 show the frequency dependent propagation constant, and the complex characteristic impedance due to the conductor loss.

In this computation, 551 rectangular edge elements are used to get converged result, especially for the attenuation curve. It takes a few minutes of CPU time on a DEC AXP 3000 machine for each frequency point. The mesh region includes the interior of the microstrip line.

Example 3—Coupled Striplines: Fig. 10 depicts the geometry of four coupled striplines of finite thickness and finite conductivity. The upper and the lower ground planes are also

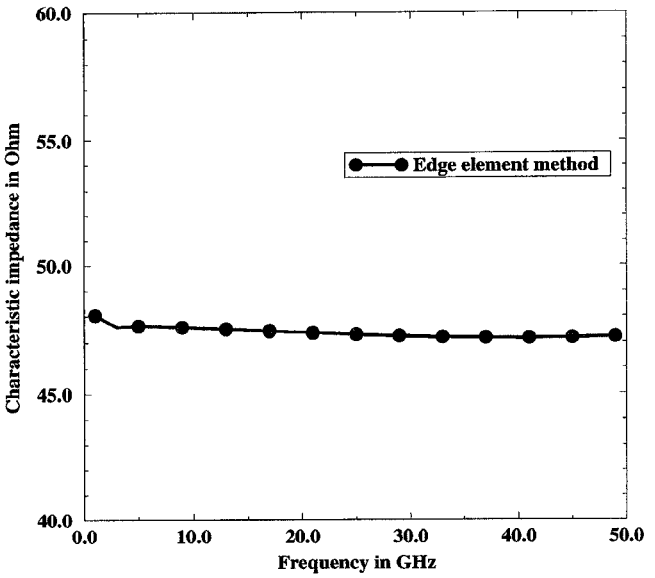

Fig. 8. Real component of the characteristic impedance of the lossy microstrip line.

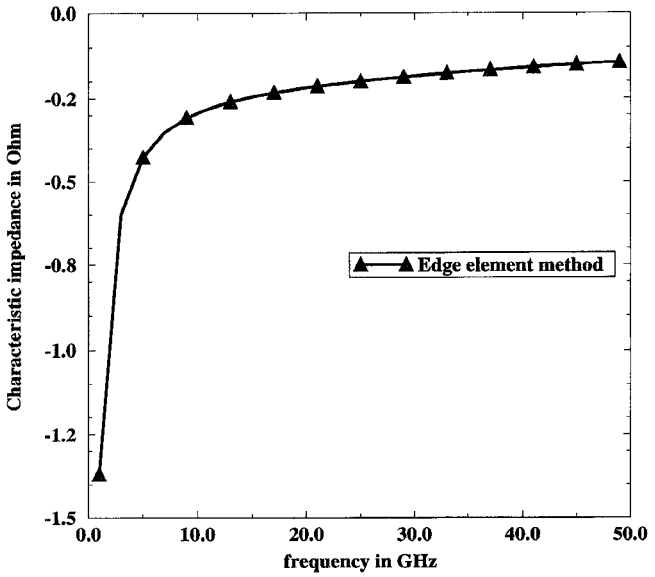

Fig. 9. Imaginary component of the characteristic impedance of the lossy microstrip line.

assumed to be lossy. Similar to the treatment in Example 2, the mesh grids pass through all the striplines. According to multiple transmission line theory, there exist four fundamental propagation modes, namely, the e-e, o-o, o-e and e-o modes.

The numerical results for the attenuation curve is displayed in Fig. 11. Comparison for the attenuation constants of our results and the VIE [8] indicates that, while agreement for the e-e mode and the o-e mode is very good, the results of the other two modes demonstrate a small difference.

VII. Conclusion

In this paper, a new functional for the $2 - D\frac{1}{2}$ structures is derived and applied to the edge element analysis. Ohmic loss and dielectric loss are treated systematically and consistently

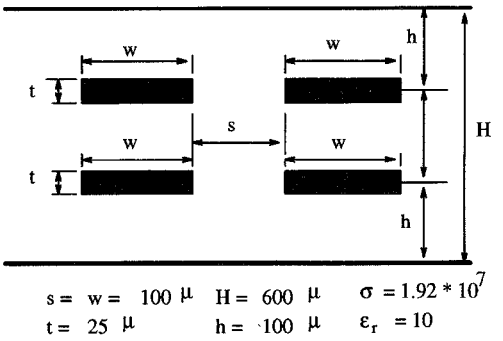

Fig. 10. Configuration of four coupled strip line structure.

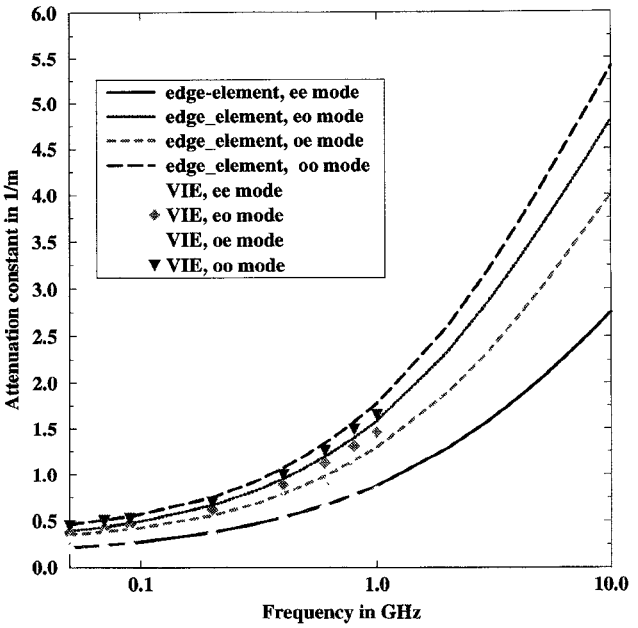

Fig. 11. Attenuation curves for the four coupled strip lines.

under the full wave regime. An extended boundary condition of the third kind is proposed and employed for the opened structures to confine the computation region with good success. The subspace iteration method is used to handle large scale generalized complex eigenvalue problems. Numerical examples of waveguides and transmission lines for digital and millimeter wave applications are presented.

Acknowledgment

The authors wish to thank J. Murphy, DARPA/ESTO, R. Pohanka and L. Kabacoff, ONR, P. Young, Boeing High Technology Center, for support and helpful discussions.

References

[1] B. K. Gilbert and G. W. Pan, "Signal processors operating at clock rates above 200 MHz," *J. Microelectronics Sys. Integration*, vol. 1, no. 2, pp. 143–160, 1993.

[2] C. Hsu *et al.*, "Analysis of multiconductor transmission lines of arbitrary cross section in multilayered uniaxial media," *IEEE Trans. Microwave Theory Tech.*, vol. MTT-41, no. 1, pp. 70–78, Jan. 1993.

[3] G. Pan, K. Olson. and B. Gilbert, "Frequency-domain solution for coupled striplines with crossing strips," *IEEE Trans. Microwave Theory Tech.*, vol. 39, pp. 1013–1017, June 1991.

[4] G. Pan, G. Wunsch, and B. Gilbert, "Frequency-domain analysis of coupled nonuniform transmission lines using Chebyshev pseudo-spatial techniques," *IEEE Trans. Microwave Theory Tech.*, vol. 40, pp. 2025–2033, Nov. 1992.
[5] R. Harrington, *Field Computation by Moment Methods*. New York: Macmillan, 1968.
[6] V. K. Tripathi and H. Lee, "Spectral domain computation of characeristic impedances and multiport parameters of multiple coupled microstrip lines," *IEEE Trans. Microwave Theory Tech.*, vol. 37, pp. 215–221, 1989.
[7] F. Olyslager, N. Fache, and D. De Zutter, "New fast and accurate line parameters calculation of general multiconductor transmission lines in multilayered media," *IEEE Trans. Microwave Theory Tech.*, vol. 39, pp. 901–909, 1991.
[8] J. Kiang, "Integral equation solution to the skin effect problem in conductor strips of finite thickness," *IEEE Trans. Microwave Theory Tech.*, vol. 39, no. 3, pp. 452–460, Mar. 1991.
[9] F. Olyslager *et al.*, "Rigorous analysis of the propagation characteristics of general lossless and lossy multiconductor transmission lines in multilayered media," *IEEE Trans. Microwave Theory Tech.*, vol. 41, no. 1, pp. 79–88, Mar. 1993.
[10] G. Slade and K. Webb, "Computation of characteristic impedance for multiple microstrip transmission lines using a vector finite element method," *IEEE Trans., Microwave Theory Tech.*, vol. 40, no. 1, pp. 34–40, Jan. 1992.
[11] J. Jin, *The Finite Element Methods in Electromagnetics*. New York: Wiley, 1993.
[12] W. C. Chew and M. A. Nasir, "A variational analysis of anisotropic, inhomogeneous dielectric waveguides," *IEEE Trans. Microwave Theory Tech.*, vol. 37, no. 4, pp. 661–668, Apr. 1989.
[13] Y. Lu and F. Fernandez, "Finite element analysis of lossy dielectric waveguides," *IEEE Trans. Magnetics.*, vol. 41, no. 2, pp. 1609–1612, Mar. 1993.
[14] E. Kriezis *et al.*, "Eddy current: Theory and applications," *Proc. IEEE*, vol. 80, pp. 1559–1590, Oct. 1992.
[15] J. Lee *et al.*, "Full-wave analysis of dielectric waveguides using tangential vector finite elements," *IEEE Trans. Microwave Theory Tech.*, vol. 39, no. 8, pp. 1262–1271, Aug. 1991.
[16] J. Wang and Mittra, " A finite element cavity resonance method for waveguide and microstrip line discontinuity problems," *IEEE Trans. Microwave Theory Tech.*, vol. 42, no. 3, pp. 433–440, Mar. 1994.
[17] J. Lee, "Finite element analysis of lossy dielectric waveguides," *IEEE Trans. Microwave Theory Tech.*, vol. 42, no. 6, pp. 1025–1031, June 1994.
[18] R. E. Collin, *Field Theory of Guided Waves*. New York: IEEE Press, 1991, p. 359.
[19] J. D. Jackson, *Classical Electrodynamics*. New York: Wiley, 1975.
[20] W. Chew, *Waves and Fields in Inhomogeneous Media*. New York: Van Nostrand Reinhold, 1990.
[21] J. Tan and G. Pan, "Circuit parameter extraction from the field theory in the full wave analysis," in preparation.
[22] K. J. Bathe and E. L. Wilson, *Numerical Methods in Finite Element Analysis*. Englewood Cliffs, NJ: Prentice-Hall.
[23] F. A. Fernandez, "Sparse matrix eigenvalue solver for finite element solution of dielectric waveguides," *Electronics Lett.*, vol. 27, no. 20, pp. 1824–1826, Sept. 1991.
[24] EMAS software, MacNeal-Schwendler Corporation, 4300 Brown Deer Road, Suite 300, Milwaukee, WI 53223 USA.

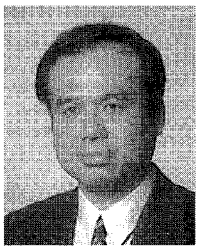

Jilin Tan received the M.S. degree in theoretical physics from Beijing Normal University, China in 1986, the M.S. degree in 1991, and the Ph.D. degree in 1995 both in electrical engineering from the University of Wisconsin, Milwaukee.

He was a Teaching Assistant from 1980 to 1983 and a Lecturer from 1986 to 1989 in the Department of Physics, Shandong Normal University, China, where he was responsible for teaching and research of electromagnetism, electrodynamics, thermodynamics, quantum-statistical mechanics, and quantum mechanics. He has been a Research Assistant and a Research Scientist since 1989 in the Department of Electrical Engineering and Computer Science at UWM. Currently he is working at Arizona State University as a Research Assistant Professor. His main interest is in theoretical modeling of the electromagnetic behavior of VLSI integrated circuits.

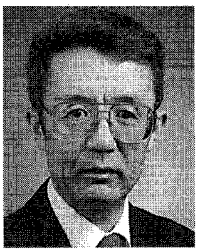

Guangwen Pan (S'81-83-M'84-SM'94) received the M.S. degree in 1982, and the Ph.D. degree in 1984 both in electrical engineering from the University of Kansas, Lawrence, KS. He came to the United States in 1980 as a graduate research assistant in the Remote Sensing Laboratory, University of Kansas.

From 1984 to 1985 he was a Post Doctoral Fellow at the University of Texas. He joined the Mayo Foundation in 1985, engaged in the theoretical modeling of the electromagnetic behavior of high-speed integrated circuits, electronic circuit boards, and high density substrates, placement and routing. From 1986 to 1988 he was with South Dakota State University as Associate Professor. From 1988 to 1995 he was with the Department of Electrical Engineering and Computer Science at the University of Wisconsin-Milwaukee as Associate Professor and promoted to Professor. He joined Arizona State University in 1995 as Professor. His research interests continue to be in the mathematical modeling of the electromagnetic environment of high clock rate signal processors.

Dr. Pan is a member of Eta Kapa Nu, and is on the Editorial Board of the IEEE/MTT.